Petroleum Science 23 (2026) 317–331

Contents lists available at ScienceDirect

Petroleum Science

journal homepage: www.keaipublishing.com/en/journals/petroleum-science

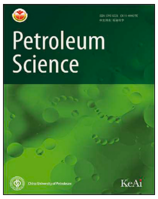

Original Paper

Insights into the evolution of pore structure and novel stress sensitivity determination of porosity-permeability in unconventional rocks

Heng Wang [a,**], Chun-Yu He [a,b], Yu-Chen Xin [a,b], Hai-Yan Zhu [b], Zhi-Wu Li [a],
Vladimir Alvarado [c,*], Lei Wang [a,b]

[a] State Key Laboratory of Oil and Gas Reservoir Geology and Exploitation, Chengdu University of Technology, Chengdu, 610059, Sichuan, China
[b] College of Energy, Chengdu University of Technology, Chengdu, 610059, Sichuan, China
[c] Department of Chemical and Biomedical Engineering, University of Wyoming, 1000 E. University Avenue, Laramie, WY, 82071, USA

ARTICLE INFO

Article history:
Received 8 May 2025
Received in revised form
22 August 2025
Accepted 24 October 2025
Available online 1 November 2025

Edited by Meng-Jiao Zhou

Keywords:
Stress sensitivity model
Pore structure
Porosity
Permeability
T_2 distribution
Deformation mechanism

ABSTRACT

The sensitivity of petrophysical parameters such as porosity and permeability to stress conditions is critical in unconventional reservoir management. Calculation of these dependencies on stress conditions that arise during oil and gas production operations remains a challenge, and despite its importance, is still poorly understood. This study focuses on the quantification of stress-dependent porosity and permeability evolution based on pore size distributions, and validation of the proposed model. To better understand the pore structure dynamic evolution and link it to rock properties, i.e. pore type, shape, and mineral composition, two tight sandstone and two shale rock samples were characterized. First, samples were assessed via Field Emission-Scanning Electron Microscopy (FE-SEM). Then, porosity and permeability were measured at different confining pressures. As proxy for the pore structure, the pore-size distribution (PSD) was determined via interpretation of the nuclear magnetic resonance (NMR) T_2 distribution. Results show that porosity and permeability decrease as the effective stress is increased, as anticipated. The detailed analysis shows that this dependence is dominated by the percentage of clay and organic matter, and the initial microstructure. Here, we proposed a connection between rock microstructure and petrophysical properties that relies on PSD, which in turn connects the T_2 distributions to stress-dependent porosity and permeability. The proposed stress sensitivity model that accounts for changes in PSD agrees well with the experimental data, better than predictions using other models. Our findings contribute to the understanding of dynamic rock petrophysical evolution and the response to the pore/fracture deformation with the adjustment of stress in subsurface activities.

1. Introduction

Rock deformation and porosity/permeability stress sensitivity are exemplified by subsurface activities such as radioactive waste disposal (Mahjoub and Rouabhi, 2018), CO_2 sequestration (Liu et al., 2021; Wang et al., 2023a), oil/gas development (Schmatz et al., 2015; Fraser-Harris et al., 2020; Yang et al., 2020), gas storage (Deng et al., 2023; Wang et al., 2023b) and reservoir evolution, e.g. tectonism and diagenesis (Wang, 2020; Li et al., 2021). During oil and gas reservoirs depletion, formation pressure declines due to fluid extraction, compression of the pore and/or fracture systems leads to a decrease in porosity and permeability. In unconventional reservoirs, i.e. tight sandstone and shale reservoirs, rock deformation that arises from production of oil and gas is more notable when compared to what is seen in their conventional counterpart. The main reason is that these less performing rocks exhibit poorer diffusion and multiphase flow (Gala and Sharma,

---

* Corresponding author.
** Corresponding author.
E-mail addresses: hwang19@hotmail.com (H. Wang), valvarad@uwyo.edu (V. Alvarado).
Peer review under the responsibility of China University of Petroleum (Beijing).

https://doi.org/10.1016/j.petsci.2025.10.023

2018; Teklu and Li, 2018). Therefore, the influence of stress on rock petrophysical properties must be understood to accurately predict fluid flow or production profiles.

The deformation of pore structures is the direct response to changes of effective stress. Previous studies have captured the changes in fracture residual width, pore morphology, and pore size using simulation and experiments. Due to the low mechanical stability, a micro-fracture is easier to close (Zhao et al., 2022). Results of 3D simulations of fracture closure shows that small features on the fracture surface contact first, followed by deformation. With the decrease of residual width and the increase of support area, fluid flow resistance increases gradually (Lu et al., 2022). For pore bodies or throats between matrix grains, as derived from digital rock analysis, the slippage, realignment, rotation and deformation of matrix grains alter the pore morphology and the pore size decreases, which tends to increase the resistance to flow (Balushi and Taleghani, 2022). Yang et al. (2020) observed morphological changes of fractures and vugs in carbonate using X-Ray computed tomography and indicated that pore throat parameters changed. Low-filed nuclear magnetic resonance (LF-NMR) is advantageous to studying changes in pore-size distribution (PSD), porosity and permeability (Zhao et al., 2023). Li et al. (2013), Chen et al. (2022) and Wang et al. (2024) used NMR to quantitatively investigate the degree of deformation for different size pores in coal, shale and sandstone samples. In addition, Xie et al. (2024) investigated T_2 spectra evolution characteristics of the different structural layers by stratified NMR technology. However, quantitative evaluation of pore structures and their influence on the rock properties for unconventional reservoir rocks, notably heterogeneous, poses a significant challenge.

For conventional reservoir rocks, the loss rate of porosity and permeability could be in the range of 10%–20% (Dong et al., 2010). In contrast, unconventional reservoirs exhibit higher porosity and permeability sensitivity to the increasing net stress upon fluid withdrawal. Moreover, the reported permeability of shale at high confining pressure could be two to three orders of magnitude lower than that at lower confining pressure (Athma et al., 2021; Zhao et al., 2022). Many empirical and theoretical relationships have been proposed, e.g. exponential, logarithmic, polynomial and power law models (Jones, 1975; McKee et al., 1988; David et al., 1994; Dong et al., 2010). For unconventional reservoirs, an exponential model has been widely employed to fit experimental data and thereby estimate the influence of stress sensitivity on oil recovery (Gala and Sharma, 2018; Wang et al., 2023c). Despite efforts to connect pore structure stress sensitivity to porosity and permeability, more work is needed.

Previous studies have shown that porosity and permeability are controlled by microscopic pore structures (Kenyon, 1992; Lai et al., 2016). Many permeability models rely on parameters such as porosity, surface area of the intergranular spaces (Kozeny, 1927; Carman, 1937), pore throat parameters derived from capillary pressure data (Rezaee et al., 2012), and tortuosity (Berg, 2014). Among them, the Kozeny-Carman equation has been widely used for permeability prediction of soils and clastic sedimentary rocks (Okazaki et al., 2014; Ren et al., 2016). However, those models were based on experimental results at ambient condition, while their suitability for the porosity/permeability stress sensitivity, especially for unconventional reservoir rocks, has not been evaluated thoroughly. Rare studies focus the quantification of stress-dependent porosity and permeability evolution based on pore size distributions. Gao et al. (2019) firstly evaluated the evolution of permeability using the Schlumberger-Doll-Research (SDR) model with the empirical constants found in previous work. For the SDR model, accurate predictions rely on the determination of empirical constants, which means that predictions are uncertain when constants without calibration are used for other unconventional reservoirs. Therefore, to eliminate the effect of rock-dependent empirical constants, new stress sensitivity models are proposed in this study based on K-C equation, McKee model and NMR results.

To evaluate the sought connection between stress conditions and petrophysical properties, NMR was used as proxy for PSD. In this order, Field Emission-Scanning Electron Microscopy is used to assess pore structure and mineral composition of two shale and tight sandstone sections. Then, porosity and permeability were measured at various effective stresses. Changes in pore structure and NMR T_2 distributions were examined. Finally, novel porosity and permeability stress sensitivity models considering PSD changes were proposed. Findings here will contribute to improving oil and gas production of unconventional reservoirs.

2. Theory

McKee's model has been widely used for various rock types (e.g., coal, granite, sandstone and clay). McKee et al. (1988) assumed that solid grains are incompressible and changes in porosity are caused by void space compression, which is assumed to depend exclusively on effective stress ($\Delta\sigma$). In addition, McKee incorporated the compressibility coefficient (C_p) into his models. Porosity (ϕ) can be written as:

$$\frac{\phi}{\phi_0}=\frac{\mathrm{e}^{-C_\mathrm{p}\Delta\sigma}}{1-\phi_0\left(1-\mathrm{e}^{-C_\mathrm{p}\Delta\sigma}\right)} \tag{1}$$

where ϕ_0 is porosity at the initial stress, MPa; C_p is the average porosity compressibility, MPa^{-1}. Based on the Kozeny-Carman equation (Zhang et al., 2018) and Eq. (1), permeability (k) can be written as:

$$\frac{k}{k_0}=\frac{\mathrm{e}^{-3C_\mathrm{p}\Delta\sigma}}{1-\phi_0\left(1-\mathrm{e}^{-C_\mathrm{p}\Delta\sigma}\right)} \tag{2}$$

where k_0 is the permeability at the initial stress, mD. The porosity compressibility (C_p) in Eqs. (1) and (2) is expressed as (David et al., 1994):

$$C_\mathrm{p}=-\frac{1}{\phi}\frac{\mathrm{d}\phi}{\mathrm{d}\sigma} \tag{3}$$

In the Kozeny capillary model, the expression of porosity is defined as (Tiab and Donaldson, 2015):

$$\phi=n\pi r^2 \tag{4}$$

where n is the pore number per unit cross-sectional area, and r is the pore radius. Combining Eqs. (3) and (4), C_p can be derived as (Zhang et al., 2018):

$$C_\mathrm{p}=-\frac{2}{r}\frac{\mathrm{d}r}{\mathrm{d}\sigma} \tag{5}$$

For water-saturated rock samples, three independent relaxation mechanisms exist for T_2: bulk relaxation time ($T_{2\mathrm{B}}$), diffusive relaxation time ($T_{2\mathrm{D}}$), and surface relaxation time ($T_{2\mathrm{S}}$):

$$\frac{1}{T_2}=\frac{1}{T_{2\mathrm{B}}}+\frac{1}{T_{2\mathrm{D}}}+\frac{1}{T_{2\mathrm{S}}} \tag{6}$$

For water-saturated rock samples, $T_{2\mathrm{B}}$ and $T_{2\mathrm{D}}$ are much larger than $T_{2\mathrm{S}}$ in the fast-diffusion regime. In the limit where T_2 is dominated by surface relaxation, $T_{2\mathrm{S}}$ can be approximated as:

$$\frac{1}{T_2} \approx \frac{1}{T_{2S}} = \rho_2 \left(\frac{S}{V}\right) \tag{7}$$

where ρ_2 is the surface relaxation rate, μm/ms; S/V is the surface volume ratio, μm^{-1}. As the ratio S/V is proportional to pore size, T_2 distribution can reflect the pore-size distribution.

In Eq. (5), C_p is converted to a parameter related to the pore diameter of the rock samples. As pore number (n) is eliminated by cancellation, pore radius (r) actually represents the average pore diameter. The geometric mean of T_2 $\left(T_{2gm}^{m}\right)$, which also represents the average pore size of the sample, is defined by (Kleinberg, 1996):

$$T_{2gm}^{m} = e^{\frac{\sum_{i=1}^{n}[P_i \ln(T_{2i})]}{\sum_{i=1}^{n} P_i}} \tag{8}$$

where T_{2i} is i-th T_2 component, ms, and P_i is spectral amplitude of T_{2i}. On this basis, pore radius (r) in Eq. (5) is replaced with T_{2gm}^{m}:

$$C_p = -\frac{2}{T_{2gm}^{m}(\Delta\sigma)} \frac{T_{2gm}^{m}(\Delta\sigma) - T_{2gm}^{m,0}}{\Delta\sigma} \tag{9}$$

where $T_{2gm}^{m}(\Delta\sigma)$ is the T_{2gm}^{m} value at the current effective stress, and $T_{2gm}^{m,0}$ is the T_{2gm}^{m} value at the initial effective stress. It is worth noting that T_{2gm}^{m} only represents the relative size of the pores of different samples. Further conversion is required to obtain a true average pore radius. However, conversion factor can be eliminated by cancellation in Eq. (9). Here, the new stress sensitivity models couple the McKee's model and the PSD (NMR) T_2 by combining Eq. (9), and Eqs. (1) and (2):

$$\frac{\phi}{\phi_0} = \frac{e^{2\frac{T_{2gm}^{m}(\Delta\sigma) - T_{2gm}^{m,0}}{T_{2gm}^{m}(\Delta\sigma)}}}{1 - \phi_0\left(1 - e^{2\frac{T_{2gm}^{m}(\Delta\sigma) - T_{2gm}^{m,0}}{T_{2gm}^{m}(\Delta\sigma)}}\right)} \tag{10}$$

$$\frac{k}{k_0} = \frac{e^{6\frac{T_{2gm}^{m}(\Delta\sigma) - T_{2gm}^{m,0}}{T_{2gm}^{m}(\Delta\sigma)}}}{1 - \phi_0\left(1 - e^{2\frac{T_{2gm}^{m}(\Delta\sigma) - T_{2gm}^{m,0}}{T_{2gm}^{m}(\Delta\sigma)}}\right)} \tag{11}$$

Table 1
Petrophysical parameters of sandstone and shale tested samples.

Sample type		Length, mm	Diameter, mm	Gas porosity, %	Gas permeability, mD
Sandstone	SD-1	26.31	25.08	16.21	6.61
	SD-2	26.43	25.21	13.34	2.52
Shale	SH-1	26.10	25.76	2.80	0.0038
	SH-2	25.92	25.20	7.20	0.0004

Table 2
Table of the multiple measurements of porosity and permeability of the SH-1 sample.

Physical properties	Confining pressure, MPa	Multiple measurement		
		1st	2nd	3rd
Porosity, %	0.5	2.78	2.81	2.81
	2.0	2.58	2.62	2.61
	5.0	2.40	2.43	2.43
Permeability, 10^{-3} mD	0.5	3.73	3.82	3.84
	2.0	3.05	3.12	2.75
	5.0	3.84	3.12	2.69

The sensitivity of porosity and permeability to stress conditions is one of the core issues in reservoir development and management. By quantifying the stress-dependent evolutionary laws of porosity and permeability based on pore size distributions, the new model provides a reliable tool for understanding the dynamic changes in reservoir petrophysical properties with respect to stress. The model is not only applicable to laboratory NMR evaluations, but also offers a new direction for the subsequent calculation of petrophysical parameters in complex lithology reservoirs using NMR logging data. This facilitates the extension of laboratory research findings to field logging analysis, providing more accurate technical support for reservoir evaluation in oil and gas field development and thus holding significant practical application value.

3. Materials and experimental methods

3.1. Materials

Four core samples, i.e. two shale samples and two tight sandstone samples, were selected from the Longmaxi Formation in the Sichuan Basin and the Yanchang Formation in the Ordos Basin, respectively. Core plugs, approximately 26 mm in length and 25 mm in diameter, were drilled parallel to the bed. Table 1 shows the petrophysical parameters.

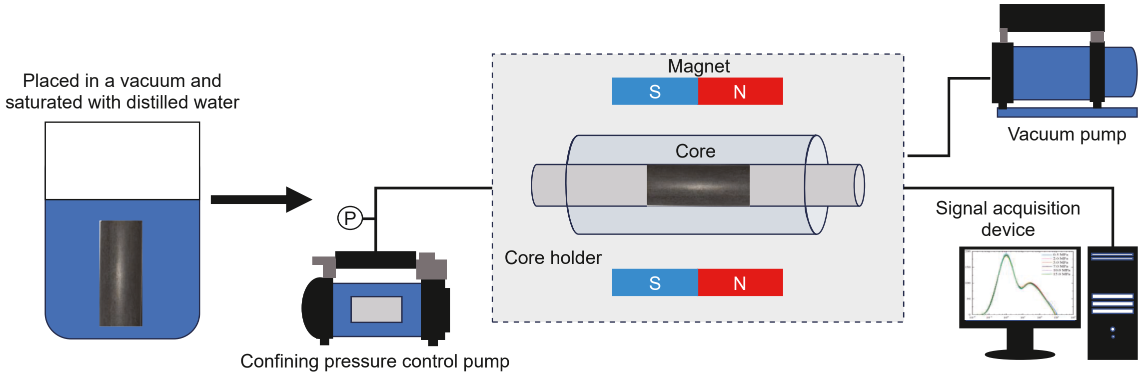

Fig. 1. NMR experimental instrument and experimental procedure.

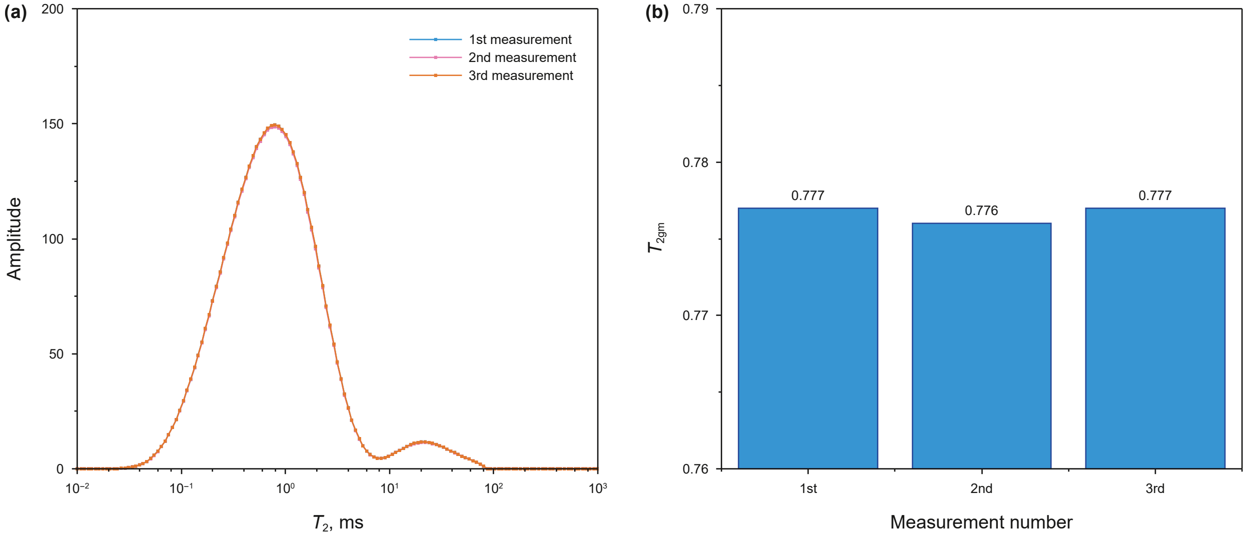

Fig. 2. **(a)** T_2 spectra by continuously measured. **(b)** Calculated T_{2gm}.

3.2. Field Emission-Scanning Electron Microscopy

To investigate the pore-fracture system and mineral composition, four thin sections (8 mm × 8 mm × 2 mm) were trimmed from core plugs ends for imaging analysis using the FE-SEM system (Quanta250 FEG). The shale sections were polished using sandpaper of different grades, followed by argon-ion polishing to create a smooth surface for high-resolution observations. In

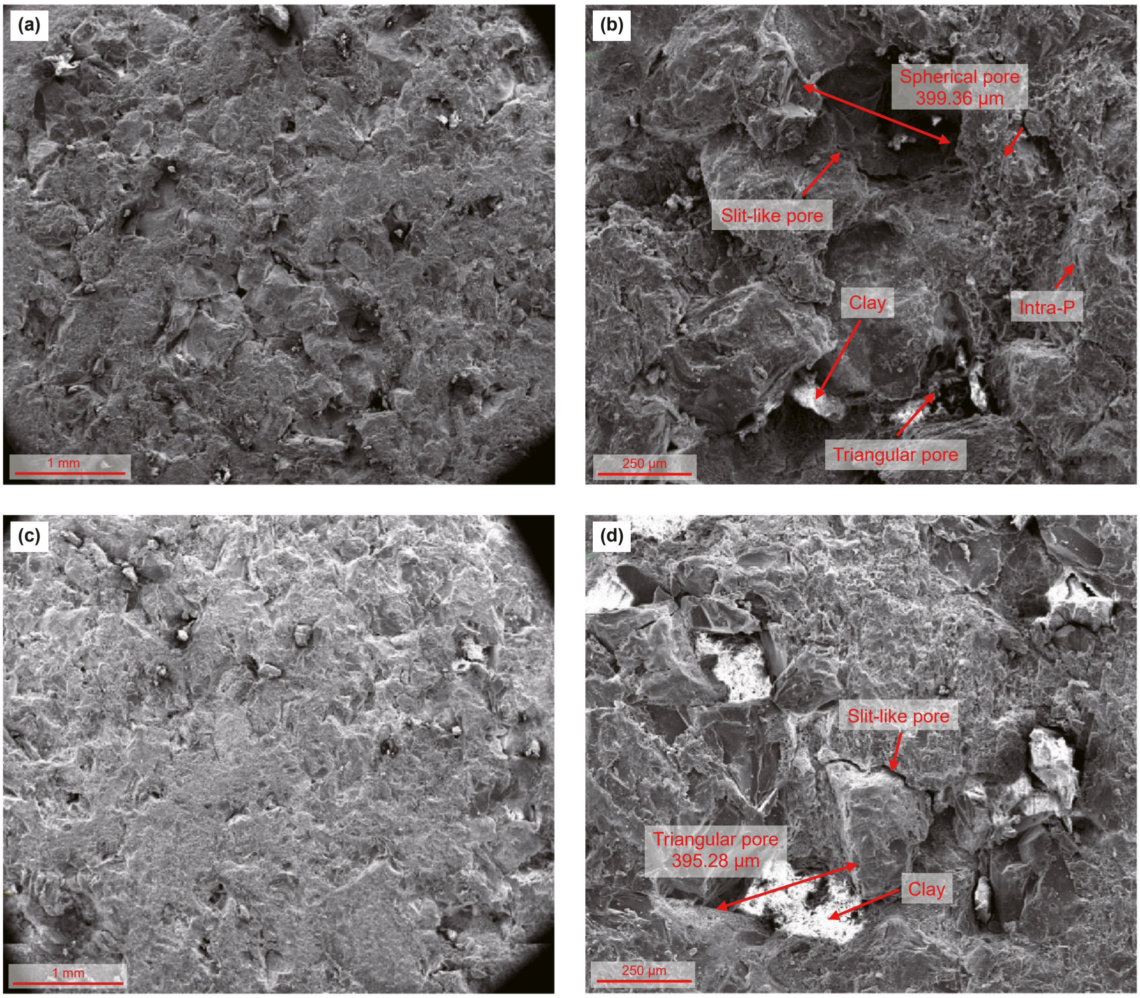

Fig. 3. **(a)** SD-1 sample SEM image; **(b)** SD-1 sample magnified SEM image. Inter-pores constitute the primary pore system; **(c)** SD-2 sample SEM; **(d)** SD-2 sample magnified SEM image. A higher concentration of clay is present in the inter-pores.

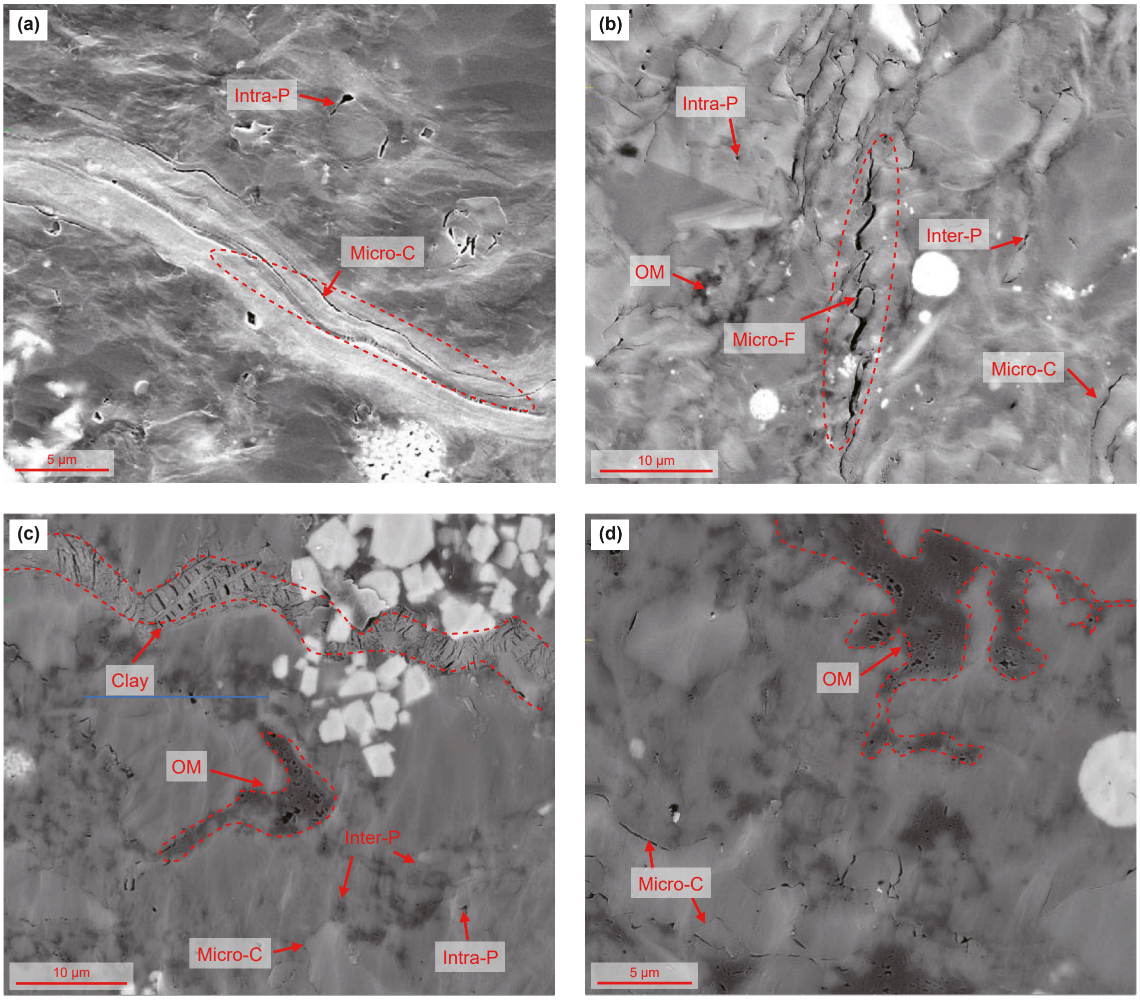

Fig. 4. **(a)**–**(b)** SEM image of the SH-1 sample. Many micro-fractures and micro-channels were found. **(c)**–**(d)** SEM image of the SH-2 sample. OM substantially contributes to the total porosity. The fracture is partly filled by clay.

contrast, the sandstone sections were observed directly without polishing.

3.3. *Porosity and permeability experiment*

For low permeability, the pressure pulse-decay technique was used (Brace et al., 1968) with helium (99.9%). Gas permeability k (in mD) is calculated as:

$$k = \frac{-s_1 \mu_g L f_z}{f_1 A P_m \left(\frac{1}{V_1} + \frac{1}{V_2}\right)} \times 0.98 \times 10^{-11} \tag{12}$$

where s_1 is the curve slope of the ln(PD) versus time, s^{-1}; μ_g is gas viscosity, Pa·s, L is the sample length, cm; f_z is the actual gas deviation value from ideal gas behavior; f_1 is the flow calibration factor; A is the cross-sectional area, cm^2; P_m is the mean pressure between upstream and downstream sides, Pa; V_1 and V_2 are the upstream and downstream reservoir volumes, cm^3.

The gas permeability of tight sandstone was measured using the steady-state flow method with nitrogen gas (99.9%) (Scheidegger, 1957). The permeability k (in mD) is calculated as:

$$k = \frac{2 q_g \mu_g L P_0}{A\left((P_1 + P_0)^2 - (P_2 + P_0)^2\right)} \times 10^2 \tag{13}$$

where q_g is the gas flow rate, mL/s; P_1 is the upstream pressure, MPa; P_2 is the downstream pressure, MPa; and P_0 is the atmospheric pressure, MPa.

The experimental procedures and precautions are as follows: Porosity and permeability were measured while the confining pressure was gradually increased step by step (0.5, 2.0, 5.0, 7.0, 10.0, 15.0, 20.0, and 30.0 MPa). At constant pore pressure, the confining pressure can be directly regarded as the effective stress. Each measurement was taken after stabilizing pressure for a minimum of 30 min. Physical properties were all measured three times under each pressure point. Taking SH-1 sample as an example, the porosity error is ±0.05%, and the permeability error is $\pm 0.1 \times 10^{-3}$ mD (Table 2). The average of the three values was calculated as the experimental value.

3.4. Nuclear magnetic resonance experiment

After the porosity and permeability experiment, the same samples were used to conducted NMR experiment. The experimental procedures and precautions are as follows: First, core plugs were vacuum-saturated with distilled water for 48 h. Samples were then placed in the core holder of the NMR spectrometer (Niumag MicroMR12-025V) (Fig. 1). The confining pressure was adjusted by increasing the pressure of fluorine oil. However, due to system limits, the effective pressure was capped at 15.0 MPa. T_2 spectra were collected 30 min after reaching stability. Parameter values using the Carr-Purcell-Meiboom-Grill (CPMG) pulse sequence were echo spacing 0.20 ms, waiting time 6000 ms, number of echoes 5000, number of scans 64.

Notably, the NMR system manufactured by Niumag Corporation demonstrated exceptional measurement precision. All instrument parameters were rigorously maintained at consistent settings. The instrument was strictly calibrated before the experiment. In addition, due to the high waiting time and number of scans, signal-to-noise ratio can reach more than 600. The triplicate measurements indicated satisfactory experimental repeatability (Fig. 2).

4. Results

4.1. Characteristics of pore structure and rock composition

Fig. 3 shows SEM images of unpolished tight sandstone sections. Two types of pores including interparticle (Inter-P) and intraparticle pores (Intra-P) are observed in SD-1 samples. Inter-pores are the dominant constituents of the pore system, commonly found between clay and quartz. Inter-pores exhibit distinct shapes, including triangles, spheres, angular shapes, and slits, with sizes ranging from tens to hundreds of micrometers (in μm). Fig. 3(b) shows that the largest spherical inter-pore can reach 399.36 μm in sample SD-1. Kaolinite and chlorite primarily exist in the inter-pores. Compared to the SD-1 sample, similar types of pores are observed in the SD-2 sample, but lower porosity, as shown in Fig. 3(a) and (c). Also, more kaolinite and chlorite primarily exist in the inter-pores of sample SD-2 (Fig. 3(d)). Additionally, intra-pores in both samples are typically located within particles and are significantly smaller compared to inter-pores.

Unlike tight sandstones, pores in organic matter (OM), micro-fractures (Micro-F), and micro-channels (Micro-C) are the main components of the pore system in shale (Liu et al., 2022). These

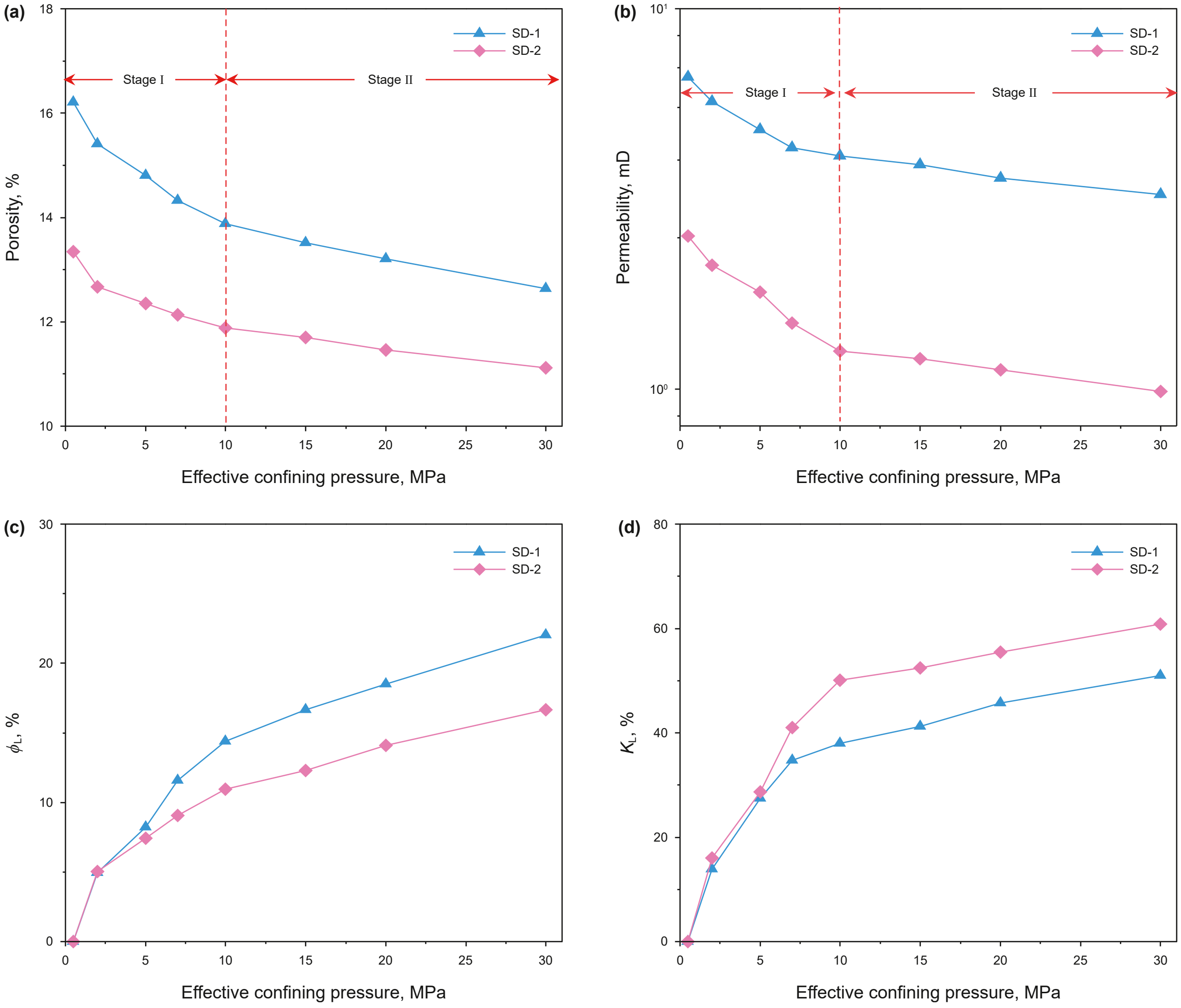

Fig. 5. Stress-dependent porosity (**a**) and permeability (**b**) of the sandstone. The loss rate of porosity (**c**) and permeability (**d**).

features are well developed in the SH-1 sample, which were formed by sedimentation and diagenesis (Fig. 4(a) and (b)). They extend far away with micro-to nano-meter openings, which develop in or on the edges of OM and minerals. For SH-2 sample, Fig. 4(c), fractures possess fragile mechanical properties and are susceptible to opening due to changes in stress conditions during deposition. Subsequently, fractures were partly quartz and clay filled, providing numerous pore spaces. OM porosity contributes substantially, especially in the SH-2 sample (Fig. 4(d)). OM is dispersed around quartz or clay minerals (light black color) and can be easily deformed into irregular shapes due to their weak mechanical properties (Chen et al., 2021).

4.2. Evolution of porosity and permeability

Fig. 5(a) and (b) show that porosity and permeability decrease as confining pressure increases. The porosity and permeability of the SD-1 sample are higher compared to those of the SD-2 sample, which agrees with the SEM observations in Fig. 3. When pressure was raised from 0.5 to 30.0 MPa, porosity and permeability of SD-1 and SD-2 samples dropped from (16.21%, 6.612 mD), (13.34%, 2.523 mD) to (12.64%, 3.242 mD), (11.12%, 0.987 mD), respectively. Furthermore, properties degraded in two stages due to the rate of porosity and permeability decline. First, their values decrease dramatically in the 0.5–10.0 MPa range. Second, porosity and permeability decrease only so slightly. To unveil the stress sensitivity, loss rates of the porosity and permeability (ϕ_L, K_L) are calculated using Eqs. (14) and (15) (Zhao et al., 2022).

$$\phi_L = \left(1 - \frac{\phi_i}{\phi_0}\right) \times 100 \tag{14}$$

$$K_L = \left(1 - \frac{K_i}{K_0}\right) \times 100 \tag{15}$$

where ϕ_L is the loss rate of porosity; K_L is the loss rate of permeability; ϕ_i is the measured porosity at current stress; K_i is the measured permeability at current stress. Although SD-1 shows a higher porosity loss rate than that of SD-2, the permeability loss rate of SD-1 is lower, which may be relevant to the pore structure and rock composition (Fig. 5(c) and (d)). The values of ϕ_L are 14.37%, 10.94%, and those of K_L are 37.99%, 50.12% in the first stage. The final values of ϕ_L are 22.02% and 16.64%, respectively, and the corresponding ones, i.e. K_L of SD-1 and SD-2, are 50.97% and 60.87%, respectively. This indicates that stress sensitivity mainly occurs at lower pressure, with permeability being more sensitive to changes in pore structure than porosity, especially for the SD-2.

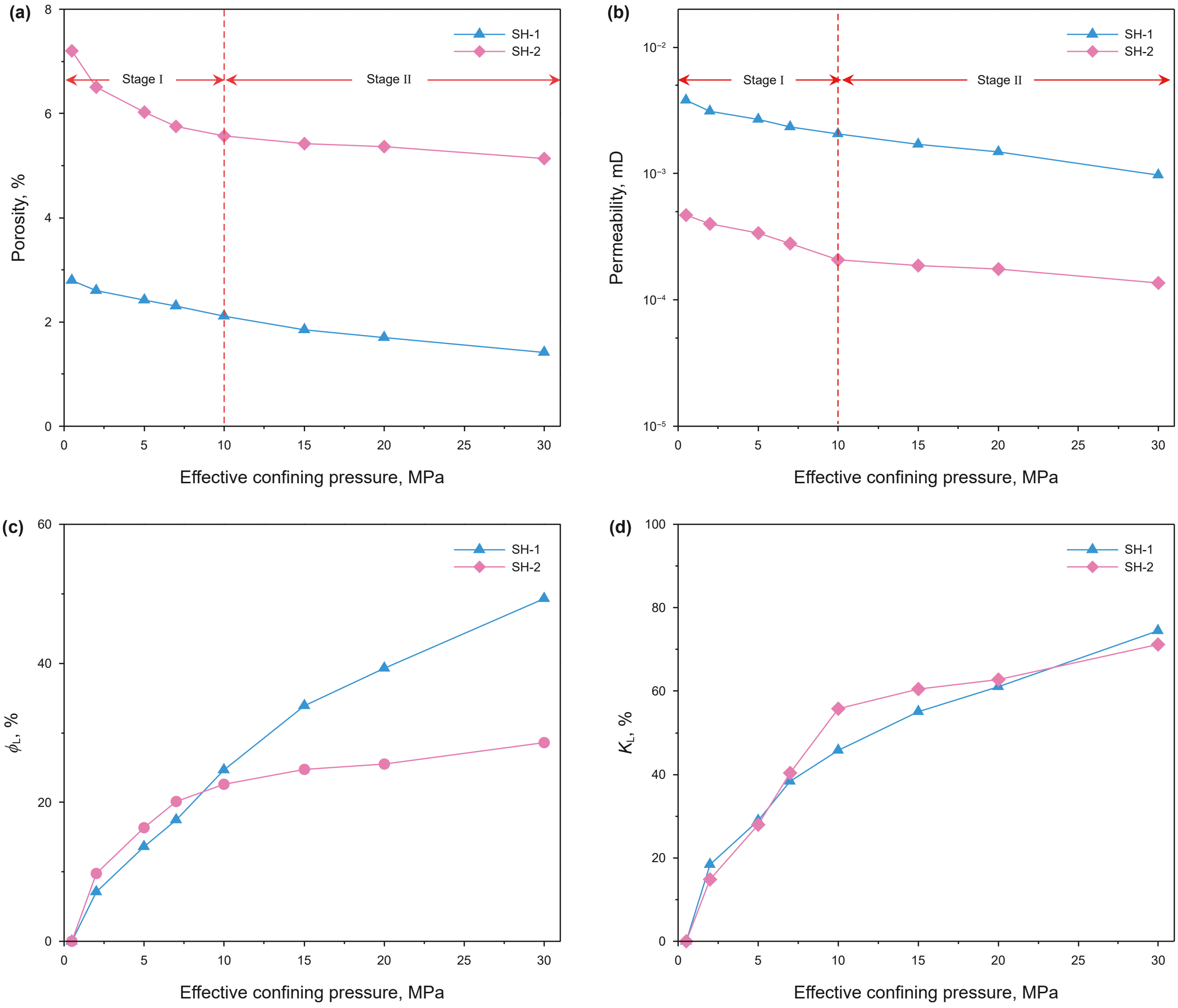

Fig. 6. Stress-dependent porosity **(a)** and permeability **(b)** of the shale; the loss rate of porosity **(c)** and permeability **(d)**.

Fig. 6(a) and (b) show the porosity and permeability evolution of two shale samples with increasing confining pressure. In contrast to the SH-2 sample, micro-fractures and micro-channels are well-developed in the SH-1 sample. Thus, the permeability of the SH-1 is larger even though its porosity is smaller. When the confining pressure increases from 0.5 to 30.0 MPa, porosity and permeability of SH-1 and SH-2 samples reduced from (2.80%, 3.800×10^{-3} mD), (7.20%, 0.470×10^{-3} mD) to (1.42%, 0.969×10^{-3} mD), (5.14%, 0.136×10^{-3} mD), respectively. Like the behavior observed in tight sandstones, SH-2 porosity and permeability trends exhibit two distinct stages. In contrast, SH-1 porosity and permeability decline in one stage. The values of ϕ_L and K_L are calculated using Eqs. (14) and (15) (Fig. 6(c) and (d)). The final values ϕ_L and K_L are (49.28%, 28.63%), and (74.51%, 71.14%), indicating that stress sensitivity for shale samples, is more noticeable than those of tight sandstone samples, agreeing with results from previous studies (Dong et al., 2010).

4.3. Evolution of T_2 distribution

T_2 distributions of water-saturated samples are shown in Fig. 7. The T_2 distributions of the SD-2 sample exhibit continuous bimodal characteristics (Fig. 7(b)), corresponding to the small and medium-large pores, respectively. However, due to the presence of more large pores in the SD-1 sample (Fig. 3(b)), the T_2 distributions exhibit continuous trimodal characteristics (Fig. 7(a)). As confining pressure increased from 0.5 to 15.0 MPa, the areas under the T_2 distribution for both samples decreased, and the whole T_2 distribution slightly shifted to the left. To quantitatively investigate the evolution of different types of pores, a parameter S is defined as:

$$S = \frac{S_i}{S_0} \tag{16}$$

where S_i is the peak area of the T_2 spectrum at the current stress; S_0 is the area under the peak of the T_2 spectrum at the initial stress. A higher value of S indicates that the stress sensitivity of a rock sample is lower. The T_2 distributions of the two tight sandstone samples can be divided into three parts, comprising small pores (<10 ms), medium pores (10–200 ms), and large pores (>200 ms), respectively. The changes in T_2 area of different types of pores are shown in Fig. 7(c) and d. The value of S for large pores can be reduced to 0.75–0.80, while the values of S for small and medium pores are over 0.90, indicating that large pores exhibit higher stress sensitivity. Similar to the evolution of porosity and

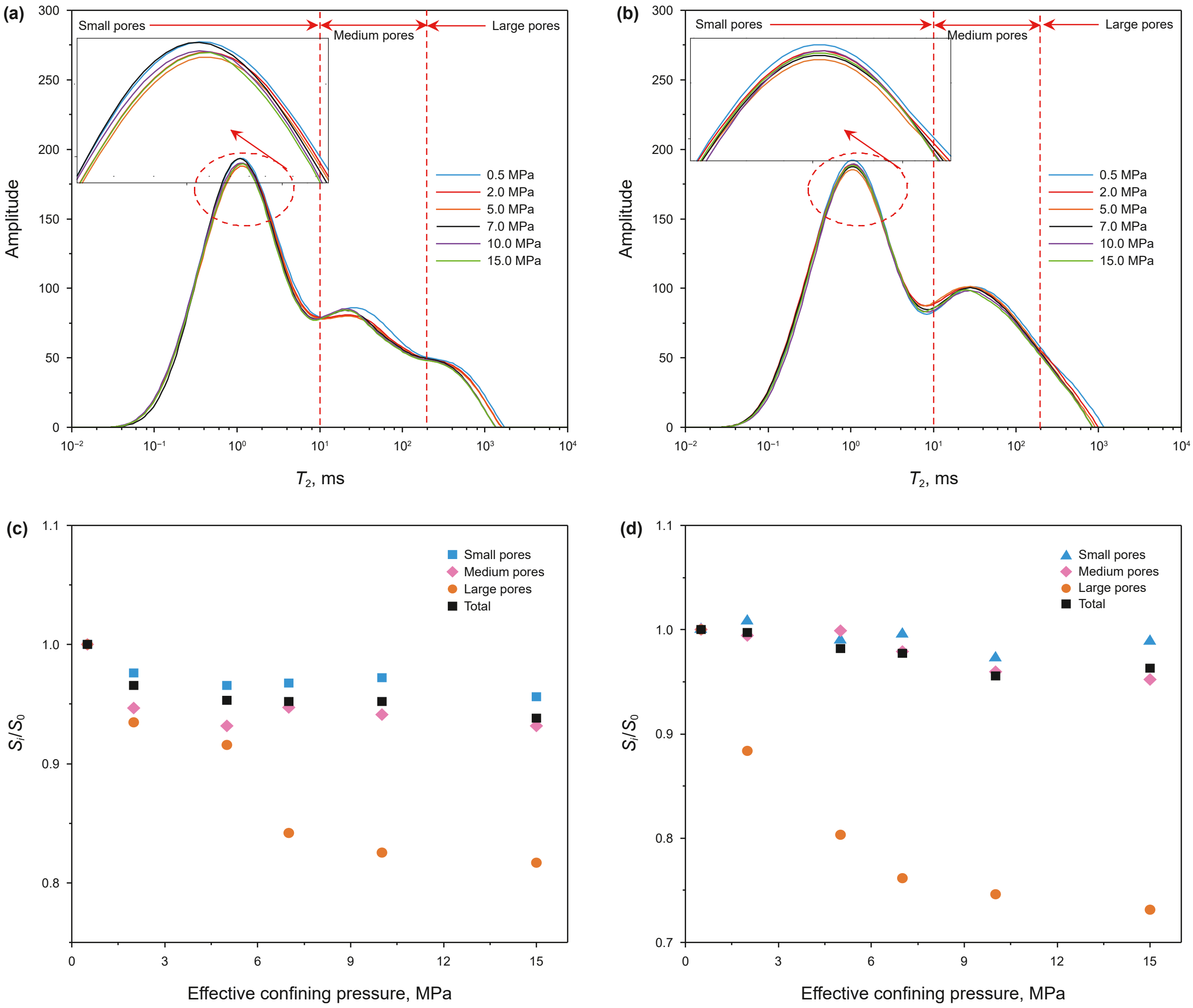

Fig. 7. T_2 spectra of two tight sandstone samples under different effective confining pressures. **(a)** SD-1 shows continuous trimodal characteristics; **(b)** SD-2 show continuous bimodal characteristics; **(c)** T_2 areas change of different pores in SD-1; **(d)** T_2 areas change of different pores in SD-2. The higher values of S, the lower stress sensitivity.

permeability, the value of S for large pores also exhibits two stages, including a rapid-decreasing stage and a slow-decreasing stage (Fig. 5(a) and (b)). However, small and medium pores show more complex changes. When the pressure exceeds 7.0 MPa in SD-1 and 2.0 MPa in SD-2, the value of S for small and medium pores slightly increases, due to the transformation of pores.

The T_2 distributions of water-saturated shale samples are shown in Fig. 8. The distribution for the SH-1 sample has two independent peaks (Fig. 8(a)). The left and right peaks correspond to the pore and micro-fracture spaces, respectively. As the porosity of the SH-1 mainly consists of pore spaces, the area under the left peak is larger than that under the right peak. Despite the higher organic matter content in the SH-2 sample, fractures are undeveloped, resulting in the weak bimodal characteristics (Fig. 8(b)). Similarly, the T_2 distribution can be divided into two parts, including small pores (<10 ms) and micro-fractures (>10 ms) for SH-1, and small pores (<0.8 ms) and medium-large pores (>0.8 ms) for SH-2. The values of S for different pores are shown in Fig. 8(c) and (d). For SH-1, when the pressure exceeds 2.0 MPa and 7.0 MPa, S of micro-fractures decreases dramatically, showing a ladder pattern during the pressurization process. Similar to the large pores of the tight sandstone samples, the S of small pores show two stages in SH-1. While for SH-2, the values of S and variation trend for small and large pores are similar, indicating that they were compressed simultaneously.

5. Discussions

5.1. Links between dynamic evolution of pore structure and rock properties

During the initial stage of stress application, some matrix grains or frame structures with low mechanical stability deform first, leading to the rapid decrease of porosity. For example, the support area of slit-like pores is susceptible to deformation, causing the pores to be compressed (Fig. 9(a)). Additionally, quartz grains in the sandstone could migrate or slip, especially for samples consisting of larger pores or more inter-pores. As stress propagates through contact points between quartz grains, the quartz grains with less contacts could easily slip to pore spaces until mechanical stability is reached. For SD-2, clay is primarily distributed in the inter-pores, as shown in Fig. 3(b). When the quartz grains are close to each other, clay can be pushed into neighbor spaces (Fig. 9(b)). Although porosity is affected slightly

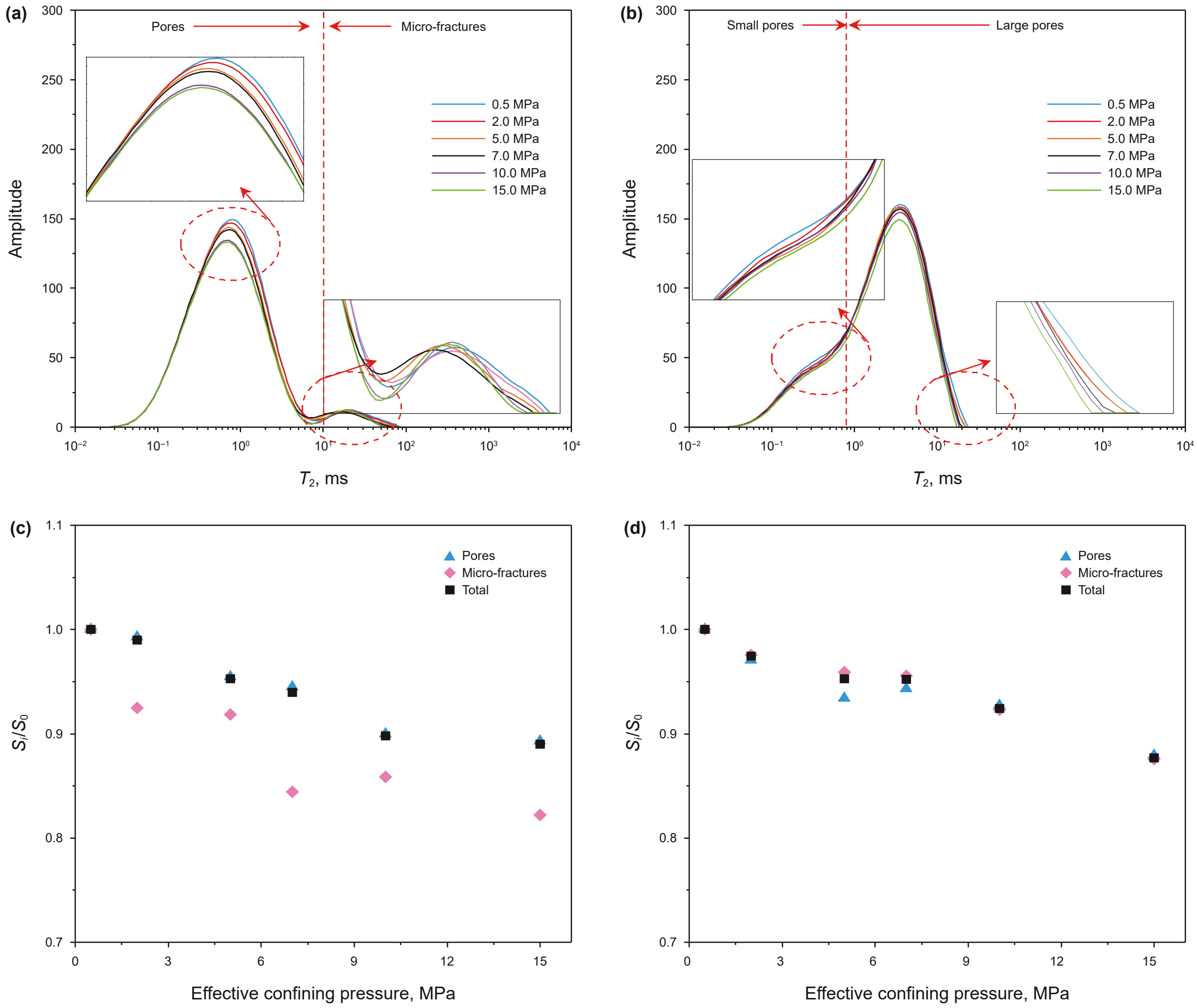

Fig. 8. T_2 spectra of two shale samples under different effective confining pressures. **(a)** SH-1 shows independent bimodal characteristics; **(b)** SH-2 shows weak bimodal characteristics; **(c)** T_2 areas change of different pores in SH-1; **(d)** T_2 areas change of different pores in SH-2. The higher values of S, the lower stress sensitivity.

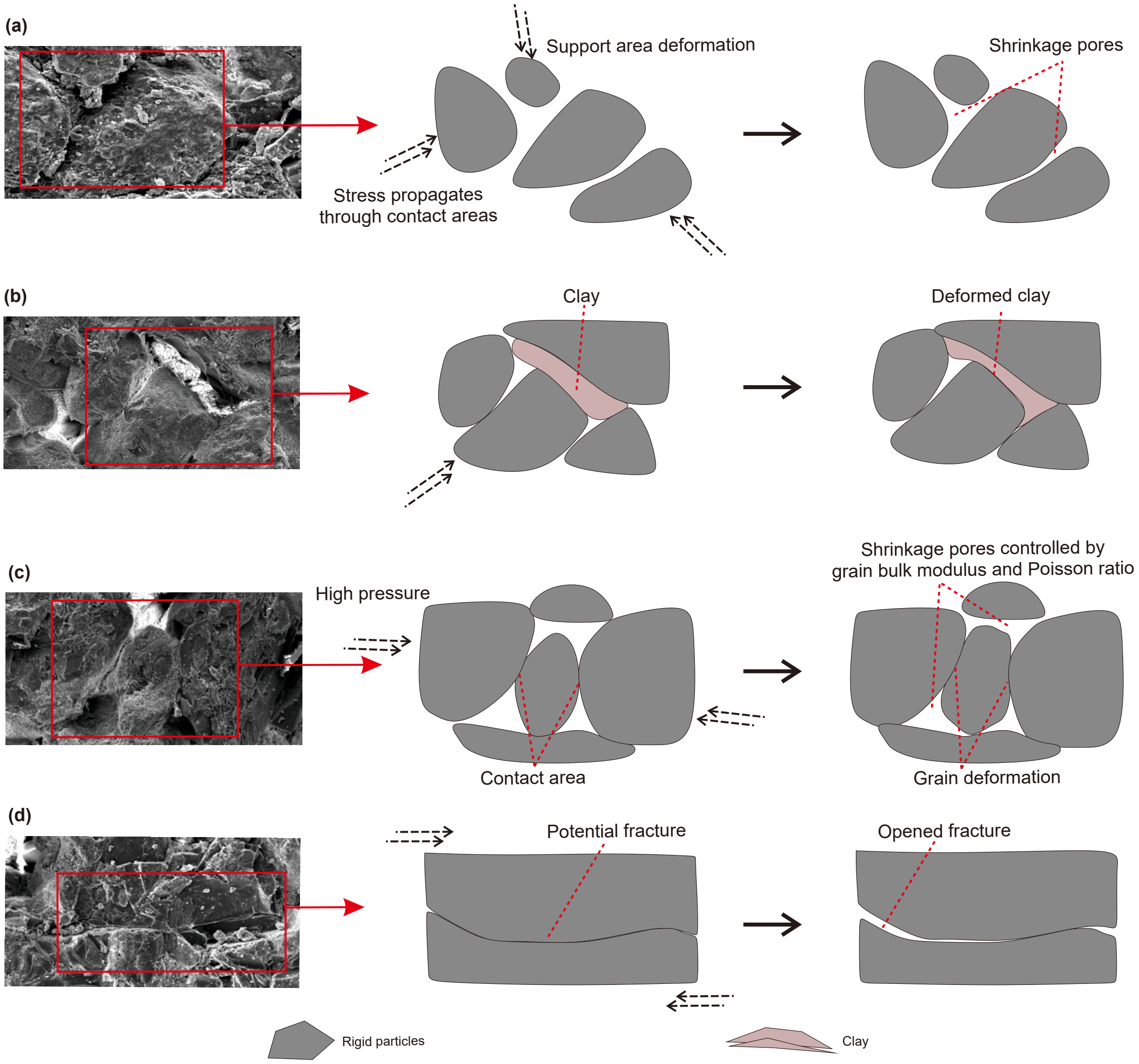

Fig. 9. Pore deformation mechanisms of the tight sandstone samples. **(a)** The support area of slit-like pores is susceptible to deformation, causing the pores to compress. **(b)** Clay is compressed due to the migration of quartz grain. **(c)** The deformation of quartz grain. **(d)** The deformation of potential fracture.

during this situation, the connectivity of pores could be significantly decreased, which explains that the permeability loss for the SD-2 sample (higher clay content) is larger (Fig. 5(d)). In the second stage, the easily deformed pores become stable, which makes the porosity slowly decrease. The contacts between quartz are compressed, and this deformation is generally elastic and reversible (Fig. 9(c)). Meanwhile, the intra-pores would be affected due to the deformation of the matrix grain.

Based on these deformation mechanisms, most pore spaces in sandstone are compressed, and the stress-dependent changes mainly occur in medium to large pores, as shown in Fig. 7(c) and (d). The SD-1 sample pore size is larger compared to that of the SD-2 sample, leading to a larger porosity loss for the SD-1 sample (Fig. 5(c) and (d)). Continuous compression could result in the transformation of larger pores into small to medium-sized pores, as supported by the increasing area of the T_2 distribution for small pores at certain stress conditions (Fig. 7(c) and (d)). However, the transition from larger to smaller pores is limited as the T_2 distribution of smaller pores decreases continuously. In addition, the realignment of matrix grains and the potential fracture opening would enlarge the size of smaller pores (Fig. 9(d)).

In contrast with tight sandstone, previous studies indicate that a significant reduction in permeability in shale can be mainly attributed to the closure of micro-crack networks (Kwon et al., 2004; Zhang et al., 2019). However, SH-1, with more micro-fractures, shows abnormal results in this study, reflecting the difference in pore or fracture deformation. Micro-fracture and micro-channels, which are the main pore spaces in the SH-1 sample, are in long and narrow shapes. The longer and narrower the pore, the easier it is for the entire frame structure to deform. As a result, the first significant decrease is observed at 2.0 MPa, as shown in Fig. 8(c). However, for an individual micro-fracture or micro-channel, as the residual width decreases gradually, bumps on the fracture surface contact. Then, the micro-fractures can be divided into several new elliptical spaces (Fig. 10(a)), and the compressive resistance of micro-fractures will gradually improve. This means that a higher pressure needs to be applied to compress the fracture. Thus, the *S* of micro-fracture shows a slight decrease only in the confining pressure range from 2.0 to 5.0 MPa (Fig. 8(c)). Indeed, shale rock consists of many fractures with varying apertures, dip angles, and strikes, contributing to the complexity of fracture deformation. The fractures of the studied rock samples can be compressed to different degrees and sequences. Alternatively, fracture apertures may widen

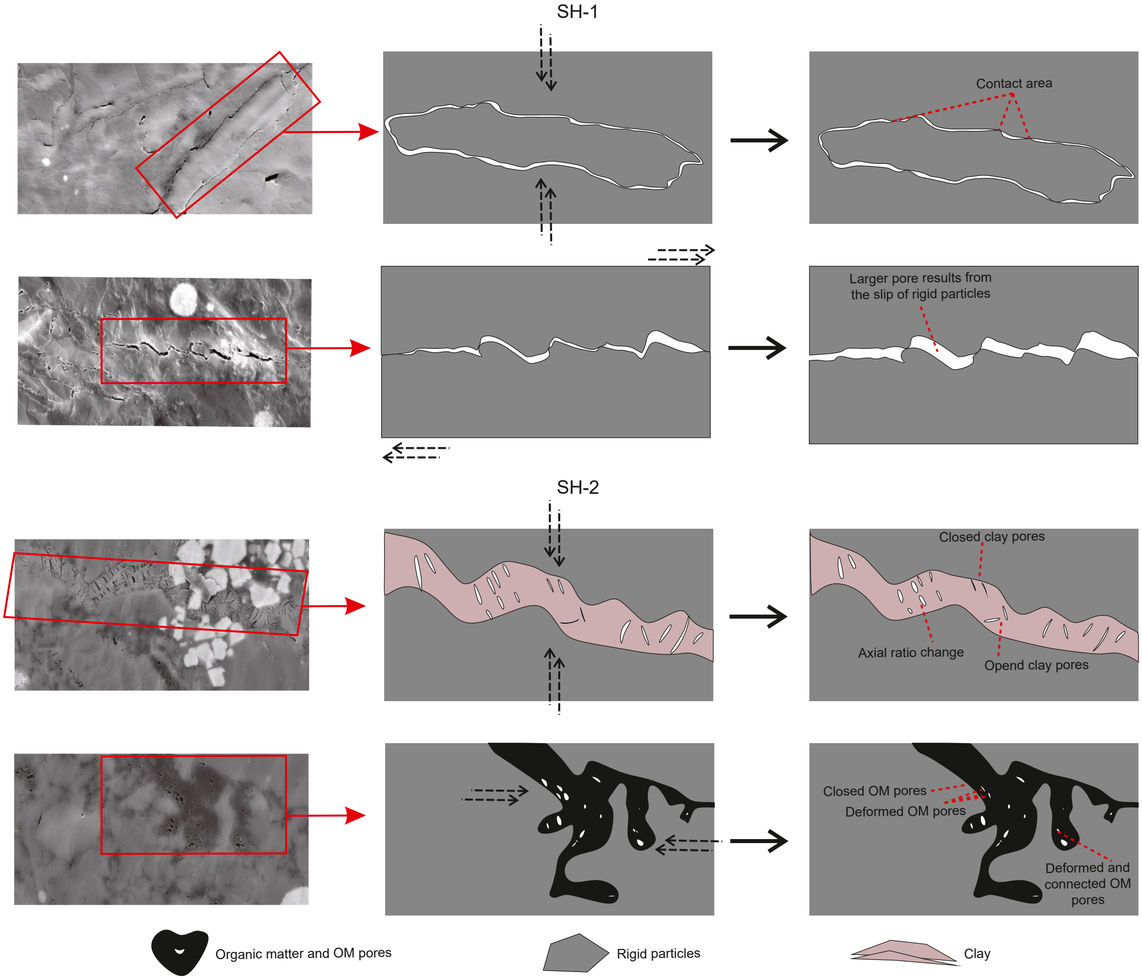

Fig. 10. Pore and fracture deformation mechanisms of the shale rock samples. **(a)** The contact area of micro-fracture increases, improving the compressive resistance. **(b)** Large pore results from the slip of matrix. **(c)**–**(d)** The deformation of clay and OM pores.

when micro-fractures are oriented perpendicular to the direction of stress. Similarly, the bumps on the fracture surface slip, or bumps with low-bearing capacity break, which also can improve pore spaces (Fig. 10(b)). This explains that the second dramatic decrease and first increase are observed at 7.0 MPa and 10.0 MPa, respectively, as shown in Fig. 8(c). This indicates that the deformation of micro-fractures has a significant influence on the porosity and permeability, and the percentage of different properties micro-fractures need to be explored thoroughly.

For the SH-2 sample, fewer micro-fractures or micro-channels were observed in the SEM images, and porosity is mainly contributed by pore spaces in the OM. Moreover, some fractures that were partially filled by quartz and clay left considerable porosity. The large percentage of OM and clay decreases the mechanical stability of the rock framework. During the pressurization, neighbor rigid particles are close to each other. The lower bulk moduli of OM and clay, which are both easier to deform, result in rapid porosity and permeability decline at the early stage (Figs. 10(c) and 9(d)). The similar values and variation trend of S obtained from the NMR T_2 distributions confirm compression of pores at all scales (Fig. 8(d)).

5.2. Porosity, permeability and stress sensitivity of models

For a fully water-saturated rock, the NMR T_2 distribution reflects the porosity and pore-size distribution, which are the theoretical basis of novel models in this study and the SDR model (Wang et al., 2018). With the increasing confining pressure, NMR results show that the T_2 distributions shrink and shift slightly leftward, indicating that pores and/or fractures can be compressed to different degrees. $T_{2\mathrm{gm}}$ at each confining pressure is calculated, which decrease with increasing pressure, reflecting the evolution of PSD (Fig. 11(a)). As larger pores are found in tight sandstones compared with shales, the decrease of $T_{2\mathrm{gm}}$ in SD-1 and SD-2 is apparent. Stress-dependent porosity and permeability have changed dramatically due to these slight changes in the pore-size distribution, evidencing a strong correlation between PSD and porosity and permeability. In addition, $T_{2\mathrm{gm}}$ shows a strong correlation with the pressure. We fitted the data using an exponential model, and the R^2 value is above 0.9, indicating a satisfactory fitting result, as shown in Fig. 11(a). By combining the evolution of PSD with initial values, the porosity and permeability at each confining stress can be calculated from Eqs. (10) and (11), as shown in Fig. (12).

For McKee's models, accurate predictions are affected by C_p. An average C_p is generally obtained by fitting the porosity measurement results or calculating based on Eq. (3). In this study, C_p is first calculated at different confining pressures (Fig. 11(b)). An average C_p is obtained based on the porosity at 0.5, 2.0, 5.0 and 7.0 MPa, resulting in values of 2.19×10^{-5}, 1.76×10^{-5}, 3.32×10^{-5}, and 4.06×10^{-5} kPa^{-1}, respectively. Then, porosity and permeability can be calculated at other confining pressures through Eqs. (1) and

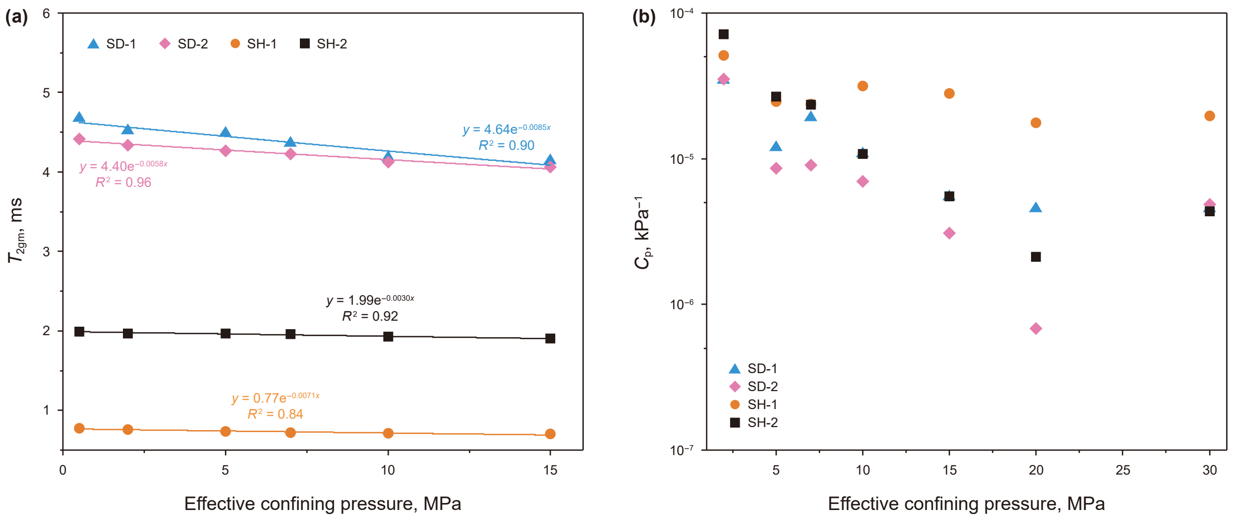

Fig. 11. **(a)** Calculated $T_{2\text{gm}}$ at different pressures. **(b)** Calculated C_P at different pressures. With the increasing of confining pressure, $T_{2\text{gm}}$ and C_P decrease.

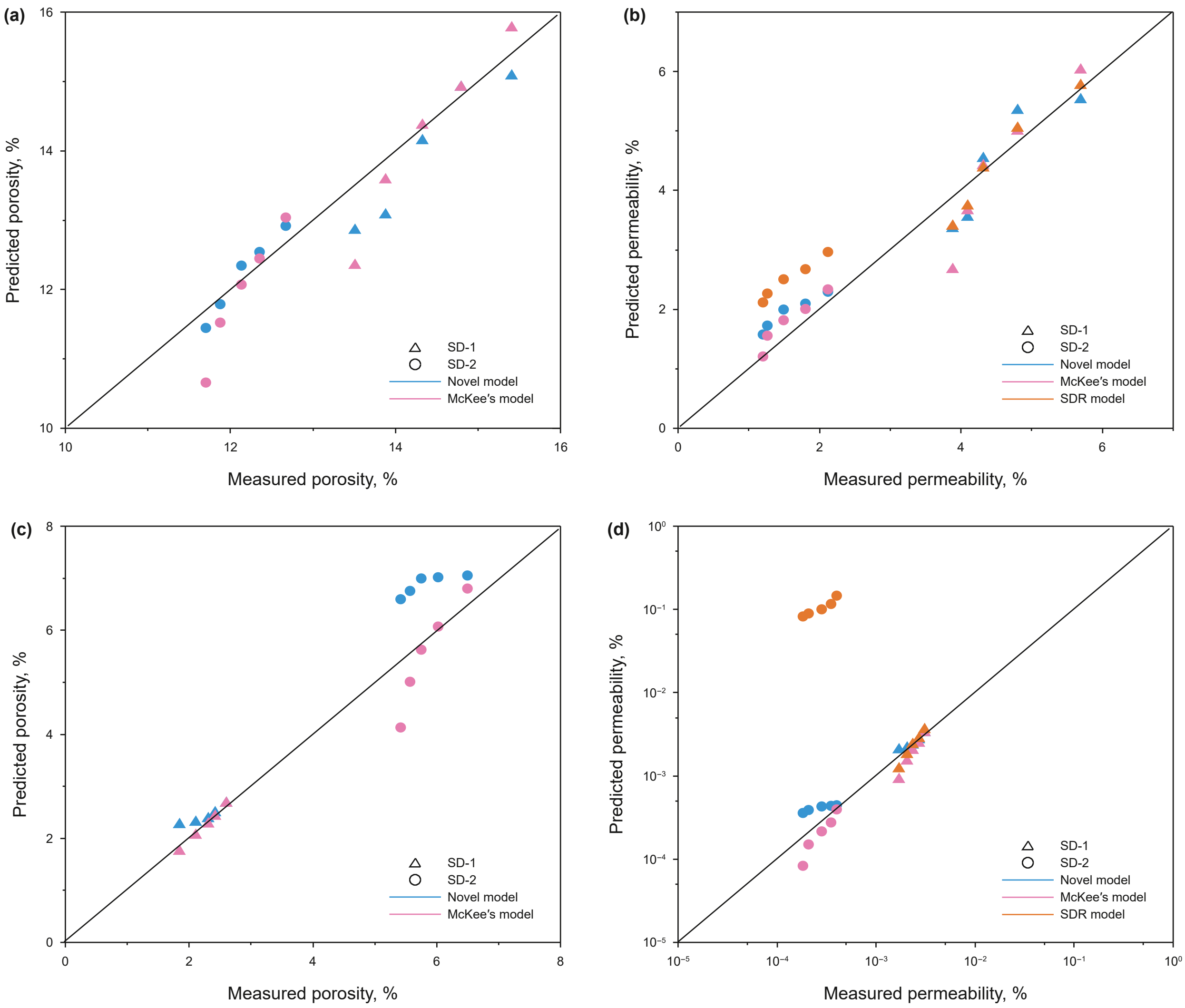

Fig. 12. Comparison of the porosity **(a)** and permeability **(b)** of the predicted and measured results for two tight sandstone samples. Comparison of the porosity **(c)** and permeability **(d)** of the predicted and measured results for two shale samples.

(2), respectively, as shown in Fig. 12. For the SDR model, an NMR-permeability equation, has been widely used in laboratory or oil filed NMR logging, as follows:

$$K = C_{\mathrm{SDR}} \times \phi_{\mathrm{NMR}}^{m} \times T_{\mathrm{2gm}}^{n} \tag{17}$$

where C_{SDR} is a formation-dependent variable; ϕ_{NMR}^{m} is the porosity; T_{2gm}^{n} is the geometric mean of T_2; m and n are empirical constants. In the SDR model, C_{SDR}, m and n need to be calibrated by experimental measurement results. In this study, the measured porosity was adopted as C_{SDR}. Referring to Gao et al. (2019), the parameters for tight sandstone samples were set as $C_{\mathrm{SDR}} = 230.0$, $m = 3.1$, and $n = 1.4$; for shale samples, the parameters were $C_{\mathrm{SDR}} = 270.0$, $m = 3.0$, and $n = 1.0$. During pressurization, porosity is gradually compressed, affecting the permeability. On this basis, the permeability under different confining pressures can be calculated, as shown in Fig. 12.

Fig. 13 shows the mean absolute percentage errors of different rocks by different models. The mean absolute percentage errors of porosity and permeability calculated by the novel models for SD-1, SD-2, SH-1, and SH-2 samples are (2.99%, 1.65%, 8.05%, 17.94%), (9.28%, 25.49%, 6.32%, 54.65%), respectively. The mean absolute errors calculated by McKee's models for SD-1, SD-2, SH-1, and SH-2 samples are (2.83%, 3.22%, 2.47%, 8.31%), (10.86%, 13.76%, 20.96%, 25.15%), respectively. The mean absolute percentage errors of porosity and permeability calculated by SDR are 5.79%, 62.64%, 12.96% and 38666.43%, respectively. The lower mean absolute percentage errors indicate that the proposed models are accurate at evaluating stress-dependent porosity and permeability. For the new models, highly accurate results were obtained as the evolution of the pore-size distribution was considered, showing that these new models provide a viable option to estimate the porosity and permeability at different pressures. For McKee's models, the absolute percentage errors at low confining pressures are relatively lower, as C_{p} is obtained based on the porosity at low confining pressures. C_{p} varies with the effective confining pressure for most rock samples, is not a constant. The early stage shows relatively higher compressibility, affecting the assessment of C_{p} (Fig. 11(b)). Therefore, the predicted porosity and permeability using the larger C_{p} values are hence lower than the measured results at high pressures. In addition, due to differences in mineral compositions and pore structures, each tested core exhibits distinct C_{p} values. To accurately predict the evolutionary characteristics of porosity and permeability for different types of cores, it is necessary to obtain corresponding C_{p} values for each, which is relatively cumbersome. For the SDR model, its prediction accuracy depends on three parameters: C_{SDR}, m, and n, involving more variables than McKee's model. In practical applications, a single set of parameters is typically used for predicting cores of the same type within the same block. For instance, in this study, we derived two sets of parameters for sandstones and shales, respectively. The prediction results for tight sandstones are better than those for shales (Fig. 12). This is because, in most cases, high porosity corresponds to high permeability, and using a single set of parameters yields satisfactory results, as exemplified by SD-1 and SD-2. However, SH-1 contains more micro-fractures, while SH-2 has poor pore connectivity, leading to an inverse relationship between porosity and permeability. Continuously using a single set of parameters under such circumstances undermines the predictive performance of the SDR model. This indicates that evaluating high-porosity, low-permeability formations remains a challenge for the SDR model. Therefore, to further improve accuracy, additional tests would be required to calibrate parameters for each individual sample. Our proposed model addresses this issue. The most critical parameter in the model is T_{2gm}, which is easily obtainable in NMR evaluations and requires no calibration.

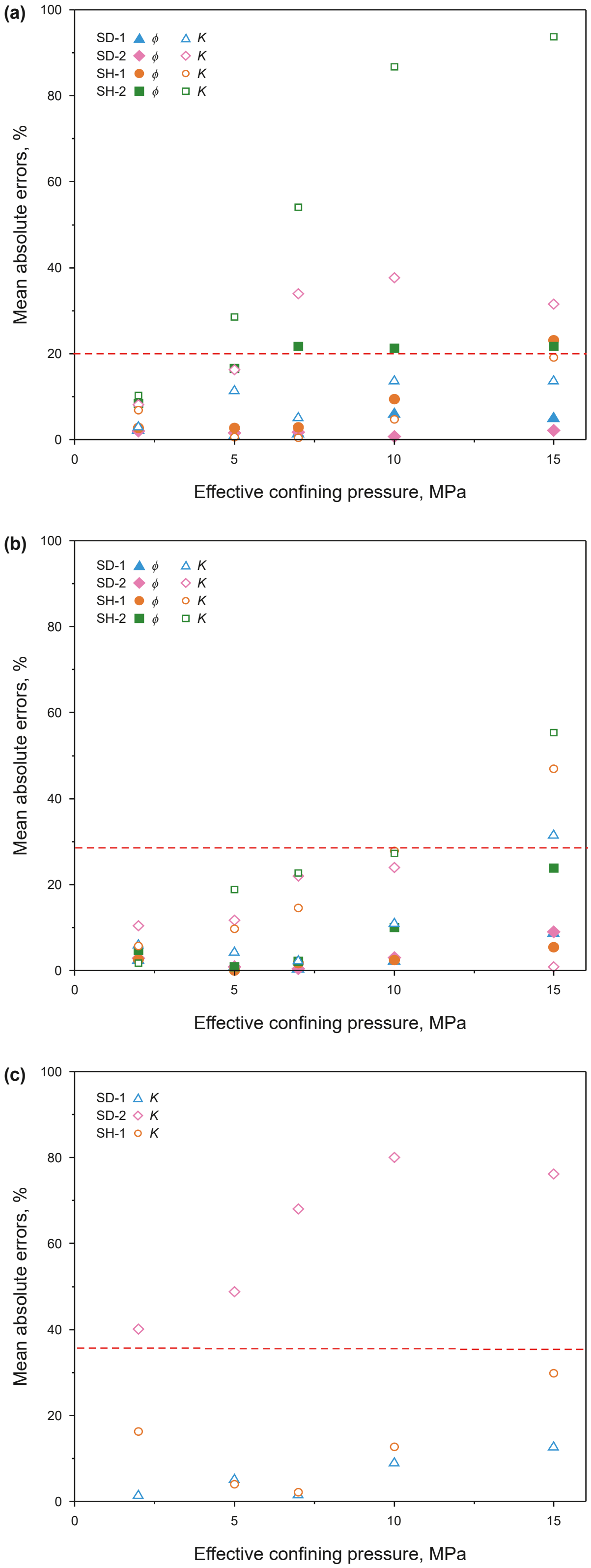

Fig. 13. The mean absolute percentage errors of porosity and permeability by different models. Novel stress sensitivity models considering **(a)** PSD, **(b)** McKee's models, **(c)** SDR model.

In summary, our study provides a method to predict porosity and permeability under different effective stresses. The predicted results are in good agreement with the experimental data and outperform those from other models. However, the model is currently only applied in laboratory NMR evaluations. In this study, the new model was developed based on experimental results of rock samples saturated with pure water, thus showing good predictive performance for water-bearing formations. In actual production, pores typically contain multiphase fluids. Different fluids may cause a shift in the T_2 geometric mean and even affect the pore closure process, thereby influencing the accuracy of prediction results, which will be investigated in our future work.

6. Conclusions

The main conclusions that derive from our results follow.

(1) Porosity and permeability decline with the increase in confining pressure due to the deformation of the pore structure. Shale samples with more micro-fractures and clay/OM show more significant stress sensitivity, particularly permeability.
(2) T_2 distributions change with the increase of the confining pressure. Sandstone sample SD-1, with medium-to-large pores, exhibits greater compressibility compared to the smaller ones (SD-2). In addition, micro-fractures in the shale sample compressed gradually with increasing confining pressure but were not completely shut due to roughness features and extended directions. Organic matter and clay have similar influence on porosity and permeability.
(3) New porosity and permeability stress sensitivity models for unconventional rocks were proposed, considering changes in pore-size distribution (T_2 distribution). In comparison to SDR model and Mckee's model, the mean absolute percentage errors of the predicted porosity and permeability estimated using the proposed models are lower, indicating the advantage of the stress sensitivity models. The strong relationship between PSD and stress provides a new way to investigate stress sensitivity.

In summary, this study focuses on the quantification of stress-dependent porosity and permeability evolution based on pore size distributions, and validation of the proposed model. Our findings highlighted challenges in linking between microscopic pore structure and macroscopic petrophysical properties, shedding light on the influence of increasing stress on unconventional reservoir rock, and henceforth its petrophysical properties alteration. Moreover, the newly proposed models provide a new quantitative way to predict the evolution of porosity and permeability, it also offers a new direction for the subsequent calculation of petrophysical parameters in complex lithology reservoirs using NMR logging data, which is key in the development of unconventional reservoirs and other subsurface activities with changing stress.

CRediT authorship contribution statement

Heng Wang: Writing – review & editing, Writing – original draft, Supervision, Resources, Project administration, Methodology, Funding acquisition, Formal analysis, Conceptualization. **Chun-Yu He:** Writing – original draft, Validation, Investigation, Formal analysis, Data curation. **Yu-Chen Xin:** Visualization, Investigation, Formal analysis. **Hai-Yan Zhu:** Visualization, Investigation, Formal analysis. **Zhi-Wu Li:** Visualization, Investigation. **Vladimir Alvarado:** Writing – review & editing, Writing – original draft, Validation, Supervision. **Lei Wang:** Visualization, Validation, Investigation.

Data availability statement

Data archived is available at https://doi.org/10.17632/6yxrmwz3n3.1.

Declaration of competing interest

The authors declare that they have no known competing financial interests or personal relationships that could have appeared to influence the work reported in this paper.

Acknowledgments

We gratefully acknowledge the financial support provided by the National Key R&D Program of China "Research and Application of Key Technical Standards for CO_2 Storage in Large Oil and Gas Reservoirs" (2023YFF0614100) and National Natural Science Foundation of China (No. 52474033). The authors would also like to thank the reviewers and editors whose critical comments were very helpful in preparing this article.

References

Athma, R.B., Peter, B.F., Ronny, H., 2021. The dependence of shale permeability on confining stress and pore pressure. J. Nat. Gas Sci. Eng. 92, 104008. https://doi.org/10.1016/j.jngse.2021.104008.
Balushi, F.A., Taleghani, A.D., 2022. Digital rock analysis to estimate stress-sensitive rock permeabilities. Comput. Geotech. 151, 104960. https://doi.org/10.1016/j.compgeo.2022.104960.
Berg, C.F., 2014. Permeability description by characteristic length, tortuosity, constriction and porosity. Transport Porous Med. 2014 103 (3), 381–400. https://doi.org/10.1007/s11242-014-0307-6.
Brace, W., Walsh, J., Frangos, W., 1968. Permeability of granite under high pressure. J. Geophys. Res. 73 (6), 2225–2236. https://doi.org/10.1016/C2009-0-64503-7.
Carman, P.C., 1937. Fluid Flow Through Granular Beds, vol. 15. Institution of Chemical Engineers, pp. 150–166.
Chen, M., Lai, Z., Kang, Y., et al., 2022. Investigation of stress sensitivity of shale nanopores via a nuclear magnetic resonance method. Energies 16 (138), 138. https://doi.org/10.3390/en16010138.
Chen, Y., Jiang, C., Leung, J.Y., et al., 2021. Multi scale characterization of shale pore-fracture system: Geological controls on gas transport and pore size classification in shale reservoirs. J. Petrol. Sci. Eng. 202, 108442. https://doi.org/10.1016/j.petrol.2021.108442.
David, C., Wong, T., Zhu, W., et al., 1994. Laboratory measurement of compaction-induced permeability changes in porous rocks-implications for the generation and maintenance of pore pressure excess in the crust. Pure Appl. Geophys. 143 (1), 425–456. https://doi.org/10.1007/bf00874337.
Deng, G., Zhou, J., Tian, S., et al., 2023. Pore structure changes and its stress-sensitive behavior in sandstone under cyclic stress: Implication for underground gas storage. Gas Sci. Eng. 119. https://doi.org/10.1016/j.jgsce.2023.205130.
Dong, J., Hsu, J., Wu, W., et al., 2010. Stress-dependence of the permeability and porosity of sandstone and shale from TCDP Hole-A. Int. J. Rock Mech. Min. Sci. 47 (7), 1141–1157. https://doi.org/10.1016/j.ijrmms.201006.019.
Fraser-Harris, A.P., McDermott, C.I., Couples, G.D., et al., 2020. Experimental investigation of hydraulic fracturing and stress sensitivity of fracture permeability under changing polyaxial stress conditions. J. Geophys. Res. Solid Earth 125, e2020JB020044. https://doi.org/10.1029/2020JB020044.
Gala, D., Sharma, M., 2018. Compositional and geomechanical effects in huff-n-puff gas injection IOR in tight oil reservoirs. Dallas, Texas, USA. In: SPE Annual Technical Conference and Exhibition, September 24–26. SPE-191488-MS.
Gao, H., Wang, C., Cao, J., et al., 2019. Quantitative study on the stress sensitivity of pores in tight sandstone reservoirs of Ordos basin using NMR technique. J. Petrol. Sci. Eng. 172, 401–410. https://doi.org/10.1016/j.petrol.2018.09.083.
Jones, F., 1975. A laboratory study of the effects of confining pressure on fracture flow and storage capacity in carbonate rocks. J. Petrol. Technol. 27 (1), 21–27. https://doi.org/10.2118/4569-PA.
Kenyon, W., 1992. Nuclear magnetic resonance as a petrophysical measurement. Nucl. Geophys. 6 (2), 153–171. https://doi.org/10.1002/cmr.1027.
Kleinberg, R., 1996. Utility of NMR T_2 distributions, connection with capillary pressure, clay effect, and determination of the surface relaxivity parameter ρ_2.

Magn. Reason. Imaging 14 (7–8), 761–767. https://doi.org/10.1016/S0730-725X(96)00161-0.

Kozeny, J., 1927. Ueber kapillare Leitung des Wassers im Boden. Sitzungsberichte Wiener Akademie 136 (2a), 271–306.

Kwon, O., Kronenberg, A.K., Gangi, A., et al., 2004. Permeability of illite-bearing shale: 1. Anisotropy and effects of clay content and loading. J. Geophys. Res. Solid Earth 109, B10205. https://doi.org/10.1029/2004JB003052.

Lai, J., Wang, G., Fan, Z., et al., 2016. Insight into the pore structure of tight sandstones using NMR and HPMI measurements. Energy Fuels 30 (12), 10200–10214. https://doi.org/10.1021/acs.energyfuels.6b01982.

Li, S., Tang, D., Pan, Z., et al., 2013. Characterization of the stress sensitivity of pores for different rank coals by nuclear magnetic resonance. Fuel, 2013 111 (1), 746–754. https://doi.org/10.1016/j.fuel.2013.05.003.

Li, X., Zhu, H., Zhang, K., et al., 2021. Pore characteristics and pore structure deformation evolution of ductile deformed shales in the Wufeng-Longmaxi formation, southern China. Mar. Petrol. Geol. 127, 104992. https://doi.org/10.1016/j.marpetgeo.2021.104992.

Liu, B., Mastalerz, M., Schieber, J., 2022. Sem petrography of dispersed organic matter in black shales: a review. Earth Sci. Rev. 224, 103874. https://doi.org/10.1016/j.earscirev.2021.103874.

Liu, J., Xie, L., He, B., et al., 2021. Influence of anisotropic and heterogeneous permeability coupled with in-situ stress on CO_2 sequestration with simultaneous enhanced gas recovery in shale: quantitative modeling and case study. Int. J. Greenh. Gas Control 104, 103208. https://doi.org/10.1016/j.ijggc.2020.103208.

Lu, C., Luo, Y., Guo, J., et al., 2022. Numerical investigation of unpropped fracture closure process in shale based on 3D simulation of fracture surface. J. Petrol. Sci. Eng. 208, 109299. https://doi.org/10.1016/j.petrol.2021.109299.

Mahjoub, M, Rouabhi, A., 2018. Modelling of anisotropic damage due to hydrogen production in radioactive waste disposal. Environ. Geotech. 5 (3), 176–183. https://doi.org/10.1680/jenge.17.00057.

McKee, C.R., Bumb, A.C., Koenig, R.A., 1988. Stress-dependent permeability and porosity of coal and other geologic formations. SPE Form. Eval. 3 (1), 81–91. https://doi.org/10.2118/12858-PA.

Okazaki, K., Noda, H., Uehara, S., Shimamoto, T., 2014. Permeability, porosity and pore geometry evolution during compaction of Neogene sedimentary rocks. J. Struct. Geol. 62, 1–12. https://doi.org/10.1016/j.jsg.2013.12.010.

Ren, X.W., Zhao, Y., Deng, Q.L., et al., 2016. A relation of hydraulic conductivity-void ratio for soils based on Kozeny-Carman equation. Eng. Geol. 213, 89–97. https://doi.org/10.1016/j.enggeo.2016.08.017.

Rezaee, R., Saeedi, A., Clennell, B., 2012. Tight gas sands permeability estimation from Mercury injection capillary pressure and nuclear magnetic resonance data. J. Petrol. Sci. Eng. 88, 92–99. https://doi.org/10.1016/j.petrol.2011.12.014.

Scheidegger, A.E., 1957. The Physics of Ow Through Porous Media. University of Toronto press.

Schmatz, J., Urai, J.L., Berg, S., et al., 2015. Nanoscale imaging of pore-scale fluid-fluid-solid contacts in sandstone. Geophys. Res. Lett. 42 (7), 2189–2195. https://doi.org/10.1002/2015GL063354.

Teklu, T.W., Li, X.P., 2018. Experimental investigation on permeability and porosity hysteresis of tight formations. SPE J. 23 (3), 672–690. https://doi.org/10.2118/180226-PA.

Tiab, D., Donaldson, E.C., 2015. Petrophysics: Theory and Practice of Measuring Reservoir Rock and Fluid Transport Properties. Gulf Professional Publishing. https://doi.org/10.1016/C2009-0-64503-7.

Wang, G., 2020. Deformation of organic matter and its effect on pores in mud rocks. AAPG Bull. 103 (1), 21–36. https://doi.org/10.1306/04241918098.

Wang, H., Alvarado, V., McLaughlin, J.F., et al., 2018. Low-field nuclear magnetic resonance characterization of carbonate and sandstone reservoirs from Rock Spring uplift of Wyoming. J. Geophys. Res. Solid Earth 123, 7444–7460. https://doi.org/10.1029/2018JB015779.

Wang, H., Xin, Y., Kou, Z., et al., 2023a. Numerical study of the efficiency of underground hydrogen storage in deep saline aquifers, rock springs uplift, Wyoming. J. Clean. Prod. 421, 138484. https://doi.org/10.1016/j.jclepro.2023.138484.

Wang, H., Kou, Z., Ji, Z., et al., 2023b. Investigation of enhanced CO_2 storage in deep saline aquifers by WAG and brine extraction in the Minnelusa sandstone, Wyoming. Energy 265, 126379. https://doi.org/10.1016/j.energy.2022.126379.

Wang, L., Wei, B., You, J., et al., 2023c. Performance of a tight reservoir horizontal well induced by gas huff-n-puff integrating fracture geometry, rock stress-sensitivity and molecular diffusion: a case study using CO_2, N_2 and produced gas. Energy 263, 125696. https://doi.org/10.1016/j.energy.2022.125696.

Wang, C., Zhang, Z., Yang, T., et al., 2024. Stress sensitivity mechanism of pores in unconsolidated sandstone reservoir using NMR technology. Geoenergy Sci. Eng. 240, 212999. https://doi.org/10.1016/j.geoen.2024.212999.

Xie, S., Zhou, H., Jia, W., et al., 2024. Spatial evolution of pore and fracture structures in coal under unloading confining pressure: A stratified nuclear magnetic resonance approach. Energy 289, 130083. https://doi.org/10.1016/j.energy.2023.130083.

Yang, Y., Tao, L., Yang, H., et al., 2020. Stress sensitivity of fractured and vuggy carbonate: An X-ray computed tomography analysis. J. Geophys. Res. Solid Earth 125 (3), e2019JB018759. https://doi.org/10.1029/2019JB018759.

Zhang, J., Wei, C., Ju, W., et al., 2019. Stress sensitivity characterization and heterogeneous variation of the pore-fracture system in middle-high rank coals reservoir based on NMR experiments. Fuel 238, 331–344. https://doi.org/10.1016/j.fuel.2018.10.127.

Zhang, W., Wang, Q., Ning, Z., et al., 2018. Relationship between the stress sensitivity and pore structure of shale. J. Inst. Gas Eng., 2018 59, 440–451. https://doi.org/10.1016/j.jngse.2018.09.010.

Zhao, P., Zeng, L., Hou, Y., et al., 2023. Experimental measurements and response analysis of resistivity of reservoirs with complex wettability: A case study of Yan'an Formation, Ordos Basin, China. Geophysics 88 (5), B195–B206. https://doi.org/10.1190/GEO2022-0456.1.

Zhao, N., Wang, L., Sm, L.Q., et al., 2022. Understanding stress-sensitive behavior of pore structure in tight sandstone reservoirs under cyclic compression using mineral, morphology, and stress analyses. J. Petrol. Sci. Eng. 218, 110987. https://doi.org/10.1016/j.petrol.2022.110987.